A micro-Raman spectroscopic investigation of He^+-irradiation damage in $LiNbO_3$

Hsu-Cheng Huang,[1,*] Jerry I. Dadap,[2] Ophir Gaathon,[2] Irving P. Herman,[2] Richard M. Osgood, Jr.,[1,2] Sasha Bakhru,[3] and Hassaram Bakhru[3]

[1]*Department of Electrical Engineering, Columbia University, New York, New York 10027, USA*
[2]*Department of Applied Physics and Applied Mathematics, Columbia University, New York, New York 10027, USA*
[3]*College of Nanoscale Science and Engineering, SUNY at Albany, Albany, New York 12203, USA*
**hh2362@columbia.edu*

Abstract: Imaging micro-Raman spectroscopy is used to investigate the materials physics of radiation damage in congruent $LiNbO_3$ as a result of high-energy (~MeV) He^+ irradiation. This study uses a scanning confocal microscope for high-resolution three-dimensional micro-Raman imaging along with reflection optical microscopy (OM), and scanning electron microscopy (SEM). The tight optical excitation beam in the Raman system allows spatial mapping of the Raman spectra both laterally and normal to the irradiation axis with ≤1 μm resolution. Point defects and compositional changes after irradiation and surface deformation including blistering and microstress are observed in the stopping region. We demonstrate that the probed area of the damaged region is effectively "expanded" by a beveled geometry, formed through off-angle polishing of a crystal facet; this technique enables higher-resolution probing of the ion-induced changes in the Raman spectra and imaging of dislocation line defects that are otherwise inaccessible by conventional probing (depth and edge scan). Two-dimensional (2D) Raman imaging is also used to determine the defect uniformity across an irradiated sample and to examine the damage on a sample with patterned implantation. The effects of different He^+ doses and energies, together with post-irradiation treatments such as annealing, are also discussed.

OCIS codes: (130.3730) Lithium niobate; (160.4670) Optical materials; (300.6450) Spectroscopy, Raman; (310.3840) Materials and process characterization.

References and links

1. L. Arizmendi, "Photonic applications of lithium niobate crystals," Phys. Status Solidi A **201**(2), 253–283 (2004).
2. J. Rams, J. Olivares, P. J. Chandler, and P. D. Townsend, "Mode gaps in the refractive index properties of low-dose ion-implanted $LiNbO_3$ waveguides," J. Appl. Phys. **87**(7), 3199–3202 (2000).
3. M. Levy, R. M. Osgood, R. Liu, L. E. Cross, G. S. Cargill, A. Kumar, and H. Bakhru, "Fabrication of single-crystal lithium niobate films by crystal ion slicing," Appl. Phys. Lett. **73**(16), 2293–2295 (1998).
4. A. Kling, M. F. da Silva, J. C. Soares, P. F. P. Fichtner, L. Amaral, and F. Zawislak, "Defect evolution and characterization in He-implanted $LiNbO_3$," Nucl. Instrum. Meth. B **175–177**(0), 394–397 (2001).
5. R. M. Roth, D. Djukic, Y. S. Lee, R. M. Osgood, S. Bakhru, B. Laulicht, K. Dunn, H. Bakhru, L. Wu, and M. Huang, "Compositional and structural changes in $LiNbO_3$ following deep He^+ ion implantation for film exfoliation," Appl. Phys. Lett. **89**(11), 112906 (2006).
6. T. Volk and M. Wohlecke, *Lithium Niobate: Defects, Photorefraction and Ferroelectric Switching* (Springer-Verlag, Berlin, Heidelberg, 2008).
7. J. E. Spanier, M. Levy, I. P. Herman, R. M. Osgood, and A. S. Bhalla, "Single-crystal, mesoscopic films of lead zinc niobate-lead titanate: Formation and micro-Raman analysis," Appl. Phys. Lett. **79**(10), 1510–1512 (2001).
8. J. E. Spanier, R. Robinson, F. Zhang, S.-W. Chan, and I. P. Herman, "Size-dependent properties of CeO_{2-y} nanoparticles as studied by Raman scattering," Phys. Rev. B **64**(24), 245407 (2001).
9. S. Banerjee, D.-I. Kim, R. D. Robinson, I. P. Herman, Y. Mao, and S. S. Wong, "Observation of Fano asymmetry in Raman spectra of $SrTiO_3$ and $Ca_xSr_{1-x}TiO_3$ perovskite nanocubes," Appl. Phys. Lett. **89**(22), 223130 (2006).
10. P. S. Dobal and R. S. Katiyar, "Studies on ferroelectric perovskites and Bi-layered compounds using micro-Raman spectroscopy," J. Raman Spectrosc. **33**(6), 405–423 (2002).
11. D. N. Jamieson, S. Prawer, K. W. Nugent, and S. P. Dooley, "Cross-sectional Raman microscopy of MeV implanted diamond," Nucl. Instrum. Meth. B **106**(1–4), 641–645 (1995).

#180352 - $15.00 USD Received 26 Nov 2012; revised 14 Dec 2012; accepted 15 Dec 2012; published 21 Dec 2012

12. A. A. Balandin, S. Ghosh, W. Z. Bao, I. Calizo, D. Teweldebrhan, F. Miao, and C. N. Lau, "Superior thermal conductivity of single-layer graphene," Nano Lett. **8**(3), 902–907 (2008).
13. I. De Wolf, "Micro-Raman spectroscopy to study local mechanical stress in silicon integrated circuits," Semicond. Sci. Technol. **11**(2), 139–154 (1996).
14. S. M. Kostritskii and P. Moretti, "Micro-Raman study of defect structure and phonon spectrum of He-implanted $LiNbO_3$ waveguides," Phys. Status Solidi C **1**(11), 3126–3129 (2004).
15. B.-U. Chen and A. C. Pastor, "Elimination of Li_2O out-diffusion waveguide in $LiNbO_3$ and $LiTaO_3$," Appl. Phys. Lett. **30**(11), 570–571 (1977).
16. J. G. Scott, S. Mailis, C. L. Sones, and R. W. Eason, "A Raman study of single-crystal congruent lithium niobate following electric-field repoling," Appl. Phys., A Mater. Sci. Process. **79**(3), 691–696 (2004).
17. K. K. Wong, ed., *Properties of Lithium Niobate* (INSPEC, The Institution of Electrical Engineers, London, UK, 2002).
18. G. R. Paz-Pujalt and D. D. Tuschel, "Depth profiling of proton exchanged $LiNbO_3$ waveguides by micro-Raman spectroscopy," Appl. Phys. Lett. **62**(26), 3411–3413 (1993).
19. A. Ofan, O. Gaathon, L. Vanamurthy, S. Bakhru, H. Bakhru, K. Evans-Lutterodt, and R. M. Osgood, "Origin of highly spatially selective etching in deeply implanted complex oxides," Appl. Phys. Lett. **93**(18), 181906 (2008).
20. A. Ofan, O. Gaathon, L. Zhang, K. Evans-Lutterodt, S. Bakhru, H. Bakhru, Y. Zhu, D. Welch, and R. M. Osgood, "Twinning and dislocation pileups in heavily implanted $LiNbO_3$," Phys. Rev. B **83**(6), 064104 (2011).
21. J. Ziegler, 2008, http://www.srim.org.
22. A. Ridah, P. Bourson, M. D. Fontana, and G. Malovichko, "The composition dependence of the Raman spectrum and new assignment of the phonons in $LiNbO_3$," J. Phys. Condens. Matter **9**(44), 9687–9693 (1997).
23. U. Schlarb, S. Klauer, M. Wesselmann, K. Betzler, and M. Wöhlecke, "Determination of the Li/Nb ratio in lithium niobate by means of birefringence and Raman measurements," Appl. Phys., A Solids Surf. **56**(4), 311–315 (1993).
24. P. Galinetto, M. Marinone, D. Grando, G. Samoggia, F. Caccavale, A. Morbiato, and M. Musolino, "Micro-Raman analysis on $LiNbO_3$ substrates and surfaces: compositional homogeneity and effects of etching and polishing processes on structural properties," Opt. Lasers Eng. **45**(3), 380–384 (2007).
25. A. Ofan, L. Zhang, O. Gaathon, S. Bakhru, H. Bakhru, Y. Zhu, D. Welch, and R. M. Osgood, "Spherical solid He nanometer bubbles in an anisotropic complex oxide," Phys. Rev. B **82**(10), 104113 (2010).
26. E. Zolotoyabko, Y. Avrahami, W. Sauer, T. H. Metzger, and J. Peisl, "Strain profiles in He-implanted waveguide layers of $LiNbO_3$ crystals," Mater. Lett. **27**(1–2), 17–20 (1996).
27. Y. Avrahami and E. Zolotoyabko, "Structural modifications in He-implanted waveguide layers of $LiNbO_3$," Nucl. Instrum. Meth. B **120**(1–4), 84–87 (1996).
28. F. Schrempel, T. Gischkat, H. Hartung, E.-B. Kley, and W. Wesch, "Ion beam enhanced etching of $LiNbO_3$," Nucl. Instrum. Meth. B **250**(1–2), 164–168 (2006).
29. Y. Kong, J. Xu, X. Chen, C. Zhang, W. Zhang, and G. Zhang, "Ilmenite-like stacking defect in nonstoichiometric lithium niobate crystals investigated by Raman scattering spectra," J. Appl. Phys. **87**(9), 4410–4414 (2000).
30. M. M. Sushchinskiy, ed., *Inelastic Light Scattering in Crystals* (Nova Science Publishers, 1987), Vol. 180, p. 81.
31. J. F. Ziegler, ed., *Handbook of Ion Implantation Technology* (Elsevier Science Publishers B.V. Netherlands, 1992), p. 13.
32. R. Srnanek, R. Kinder, B. Sciana, D. Radziewicz, D. S. McPhail, S. D. Littlewood, and I. Novotny, "Determination of doping profiles on bevelled GaAs structures by Raman spectroscopy," Appl. Surf. Sci. **177**(1–2), 139–145 (2001).
33. W. Primak, "Expansion, crazing and exfoliation of lithium niobate on ion bombardment and comparison results for sapphire," J. Appl. Phys. **43**(12), 4927–4933 (1972).

1. Introduction

Increasingly, complex oxide crystals and epitaxial thin films, with their remarkable physical properties [1], are of interest both for studies in basic condensed matter physics and for advanced microdevices such as high-performance acoustic and photonic applications. These oxide crystals, including, for example, lithium niobate ($LiNbO_3$), strontium titanate and its alloys, yttrium iron or aluminum garnet, and lanthanum aluminate, exhibit a wide variety of functionalities. In addition, the fabrication of devices from these crystals often involves their irradiation by energetic particles, including light ions. For example, He ion implantation is an important step in optical-waveguide [2] fabrication and thin-film exfoliation methods [3]. Exposure to ion bombardment is also a consideration in the performance of practical applications of devices, such as surface acoustical wave (SAW) and photonic devices, in extreme environments. Because of this widespread interest, it is crucial to achieve a clear and specific understanding of the chemical and structural response of complex oxides to ion irradiation.

Damage due to high-energy-ion exposure can be analyzed using well-developed ion-beam-probing instrumentation. This includes Rutherford backscattering spectrometry (RBS) [4], nuclear reaction analysis (NRA) [5], and particle induced X-ray emission (PIXE) [6].

#180352 - $15.00 USD Received 26 Nov 2012; revised 14 Dec 2012; accepted 15 Dec 2012; published 21 Dec 2012

These methods have been used extensively and successfully for material characterization of radiation damage, including that in complex oxides; however, these methods require extensive use of accelerator-based-beam-line systems and in-vacuum environment for experimentation. Confocal micro-Raman spectroscopy can provide an alternate approach to probing energetic ion damage and material changes; it provides a direct approach for sampling over the set of crystal vibrational normal modes and thus is sensitive to crystallinity and composition. This technique is laboratory based and can be operated at ambient atmospheric conditions with different sample configurations. In addition, the use of a tightly focused optical excitation beam, with computer control and data taking, allows mapping of the Raman spectra both laterally and normal to the irradiation axis with 1-micrometer spatial resolution. Its utility has been reported for determining the processing-induced materials properties of several complex oxides [7–9] including studying the influences of stresses and stoichiometry in lead- and barium-based ABO_3 perovskites [10] and other materials such as diamond [11–13]. In addition, Kostritskii and Moretti [14] have done pioneering work on ion damage in He-implanted $LiNbO_3$ and identified important damage effects in this material. However, despite these insights important questions remain.

In this paper, we use imaging micro-Raman spectroscopy measurements to readily analyze and characterize materials properties of an important complex oxide, i.e. $LiNbO_3$, after high-energy-ion irradiation by He^+. Thus, we utilize this method to measure local compositional changes as well the depth and depth distribution of the implanted ions. In addition, we determine the spatial resolution, crystallinity, and compositional information gathered based on three different and complementary incident optical beam/sample geometries for the previously irradiated crystal, *viz* depth profiling into the top surface of the crystal, depth profiling based on scanning laterally along a crystal edge facet, and higher-spatial-resolution depth scanning using a small-angle-beveled edge. We also use 2D imaging based on computer-controlled scanning and data processing to image the stopping region and spatial variations of damage adjacent to patterned regions, via the intensities of allowed and forbidden modes. The modal intensities at the boundary of irradiation and the implantation uniformity are also discussed. The utility of Raman scattering to optimize post-irradiation processes, such as annealing, is also shown.

2. Experimental

Congruent Z-cut $LiNbO_3$ wafers (Crystal Technology) were diced into 1 cm^2-area samples and irradiated by He^+ ions along the crystalline Z-axis with doses ranging from 10^{12} to 5×10^{16} cm^{-2} at 1.2 - 3.8 MeV energies. During the irradiation, samples were tilted at 7° from the Z axis to prevent channeling and the irradiating beam was raster scanned to achieve a uniform dose. During irradiation, the samples were water cooled to avoid overheating. Patterned irradiation was accomplished by placing a 0.5 mm-thick metal sheet with circular openings (~500 μm in diameter) on the top surface of the sample. The mask was attached to the sample at the mask periphery with silver paste with no hard contact in the center. In addition, after the irradiation, selected samples (not patterned) were annealed in a furnace at temperatures ranging from 250 - 600°C under laboratory-ambient pressure conditions. The annealing temperature was carefully adjusted to temperatures less than 800°C such that the loss of Li and oxygen were to a large extent minimized [15]. In addition to micro-Raman spectroscopy, which is the central technique for this work, the irradiated samples were investigated with optical microscopy (OM) and scanning electron microscopy (SEM).

For Raman probing, a diode-laser-based laser light source, 532 nm wavelength and 2.7 mW power, was used as the excitation source, along with a computer controlled X-Y-Z stage. The beam was focused by a 100 × microscope objective, NA = 0.85 using a confocal pinhole alignment to a spot size of 1 μm. The experiments were performed in a backscattering geometry with three different optical configurations; these are shown in Fig. 1.

The first configuration was direct, top-down probing (see Fig. 1(a)), with the incident light parallel to the Z-axis and the focus scanned along the Z-axis (depth scan); in this configuration the selection rules allowed backscattering of the E(TO) (152, 236, 263, 322,

#180352 - $15.00 USD Received 26 Nov 2012; revised 14 Dec 2012; accepted 15 Dec 2012; published 21 Dec 2012

365, 432, and 581 cm^{-1}) and A_1(LO) (274, 331, 432 and 875 cm^{-1}) phonon modes. Note that lithium niobate is in the space group *R*3c and has a distorted Perovskite-type structure. This structure should yield 13 phonon peaks for our backscattering orientation. However, for our experiments only 10 peaks are apparent, an effect explained earlier [16] as due to nonstoichiometric intrinsic defects in congruent $LiNbO_3$. The Rayleigh length was estimated to be ~2 μm. Two-dimensional imaging was also performed with this optical configuration to study the degree of uniformity of the irradiation and, on samples with the patterned implantation to examine the transition from the irradiated to unirradiated regions. Using this patterned sample, the beam was scanned over a square region containing unmasked circular regions that were irradiated. Different step resolutions were used to probe the sample, including a 640 μm × 640 μm array using with 5-μm steps, a 16 μm × 16 μm with 0.4 or 0.2 μm steps.

The second optical configuration probed (see Fig. 1(b)) along the X-axis and into an edge facet with the light perpendicular to the Z-axis and scanned along the Z-axis (edge scan); for this orientation, backscattering of the E(TO) and A_1(TO) (254, 276, 332 and 631 cm^{-1}) phonon modes is allowed. Finally the third configuration (see Fig. 1(c)) allowed interrogation of the beveled sample edges (bevel scan). In this case, the two edges of the implanted samples were carefully angle-lapped to an optical finish so as to be aligned 5° from the Z-axis (XY plane); because of the small angle of the beveling, the polarization selection rules in this case were essentially the same as for the first configuration. The sample was polished until the defect region was fully exposed at the surface. Scanning was then carried out with the polished planes oriented parallel to the stage. The sketches in Fig. 1 show clearly the three scanning directions in our experiments. Scanning was done in increments of 0.2 μm until the beam focus crossed to >2-3 μm beyond the heavily damaged region.

Note that for the depth scan, i.e. Fig. 1(a), an optical correction factor must be applied to obtain the true depth. In particular, in our measurements, we directly measured the movement of the stage and then applied a correction factor due to refractive-index alteration of the beam focus in the crystal in order to measure the actual depth inside the sample. For $LiNbO_3$, the refractive index at 532 nm, as given by Sellmeier equation [17], of $LiNbO_3$ is ~2.3, which means that, by a Gaussian ray-transfer matrix calculation, the actual probed depth was ~2.3 times larger than the measured position of the Raman microscope Z-stage.

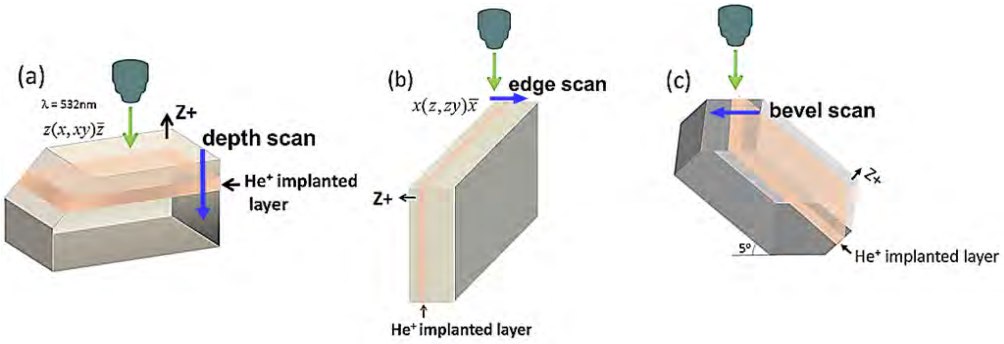

Fig. 1. Schematic of the three experimental orientations for our micro-Raman probing beam: (a) depth scan from the surface into the bulk along the Z-axis, (b) edge scan along the X-axis and (c) bevel scan along the polished side (beveled plane).

3. Results and discussion

Our experiments presented below used micro-Raman spectroscopy following irradiation of crystalline $LiNbO_3$ with ~MeV He^+ ions to probe the location of structural and chemical changes. Our presentation is organized so as to examine the resulting material changes using each of the three scanning orientations discussed above and to consider each approach in a separate section.

#180352 - $15.00 USD Received 26 Nov 2012; revised 14 Dec 2012; accepted 15 Dec 2012; published 21 Dec 2012

3.1. Depth-dependent changes in irradiated samples (depth scan)

Figure 2(a) shows the marked changes in the $LiNbO_3$ Raman spectra using the configuration of Fig. 1(a), after irradiation over a range of Raman shifts from 100 to 1000 cm^{-1}. The spectra are taken for a virgin sample, an irradiated surface, and an annealed sample; all were made with the probe focal point positioned ~10 μm beneath the surface, i.e. at the plane of the ion stopping range. The irradiation was carried out with 3.8 MeV He^+ ions at a dose of 5×10^{16} cm^{-2}. In addition, unless otherwise specified, all annealing was done at 250°C for 30 min following irradiation. Figure 2(b) shows measurements made under identical conditions, but with the focal spot positioned so that the crystal surface was sampled.

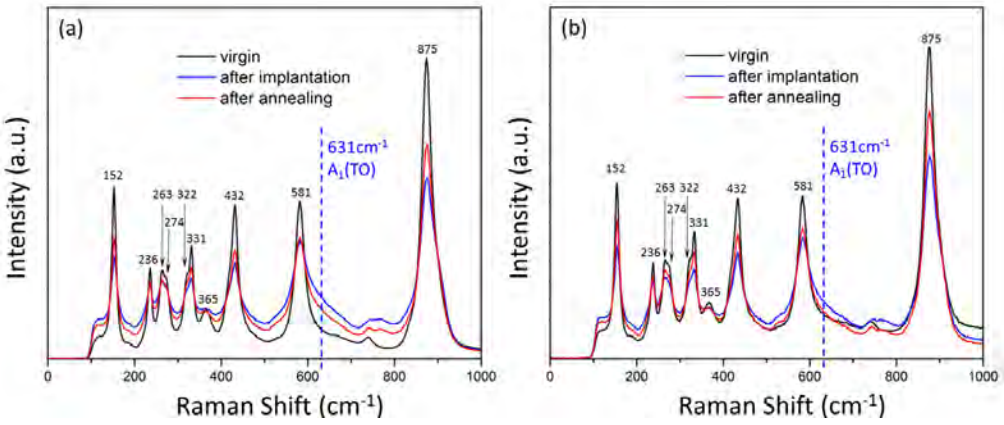

Fig. 2. Comparison of the Raman spectra made on unirradiated ("virgin") with depth scan, irradiated ("after implantation"), and post-irradiation annealed ("after annealing") samples: (a) at the depth of the ion stopping region and (b) at the surface. Furnace annealing was carried out at 250°C for 30 min. In (a), a shoulder is apparent in spectra between 600 cm^{-1} and 750 cm^{-1}.

Figure 2(a) shows that in the stopping region, after irradiation, there is in general, a substantial intensity loss in each of the backscattering-allowed modes of the irradiated crystal, along with a broadening of their line shapes. In addition, after irradiation there are also new features from 600 to 770 cm^{-1}. More subtle changes are also apparent, including a new high-frequency shoulder for the E(TO) 580 cm^{-1} peak from 600 to 700 cm^{-1} and a new feature at ~766 cm^{-1}, which is adjacent to the small intrinsic peak at ~738 cm^{-1}; the origin of these two new irradiation-induced features are discussed below. The 631 cm^{-1} "shoulder" has been previously reported and attributed to damage-induced distortion of the niobium octahedron [18], which results in changes in the Nb-O bond stretching vibrations. Note that this $A_1(TO_4)$ 631 cm^{-1} mode is forbidden in the pristine crystal for the optical configuration used for this figure. Figure 2(b) shows that these changes are also seen in the surface region, albeit to a lesser extent. The larger signal in the stopping range is due simply to the fact that for light-ion irradiation, lattice damage is the largest in the nuclear interaction region, i.e. the buried stopping range. Finally, the third spectra in Figs. 2(a) and 2(b) are obtained after low-temperature annealing; the restoration of the signal toward that of the virgin sample shows that the irradiation damage can be, in part, removed by annealing. Annealing-induced "repair" of irradiation damage of $LiNbO_3$ has been reported extensively in previous measurements [19,20]. In part this "repair" is due to diffusive dissipation of interstitial He in a heated crystal. Figure 3(a) shows the spectra of the virgin and irradiated sample from 500 to 700 cm^{-1}. It is clear that, after irradiation, the peak width of 581 cm^{-1} mode is broadened, indicating the crystal quality is affected. However, after subtracting their respective backgrounds, the integrated areas under the two curves are nearly the same. This result implies that the concentration of phonon oscillators remains largely the same after irradiation (5×10^{16} cm^{-2} He^+ dose at 3.8 MeV). Of course there is local destruction of the lattice particularly within the

#180352 - $15.00 USD Received 26 Nov 2012; revised 14 Dec 2012; accepted 15 Dec 2012; published 21 Dec 2012

ion-stopping-range region, but due to the finite resolution of depth scan, approximately that of the Rayleigh length of the focused beam, i.e. ~2 μm, the average number of oscillators, over this range is relatively unaffected. After irradiation, in addition to broadening of the 581 cm^{-1} phonon-mode linewidth, a shoulder emerges with its peak centered near the $A_1(TO_4)$ 631 cm^{-1} mode. This feature may be seen clearly by fitting the distorted feature with two Lorentzian features, as is shown in the inset of Fig. 3(a). Note that the slight shift in the fitted position (628 cm^{-1}) of this peak is consistent with a small irradiation-induced strain. Raman data such as shown in Fig. 3 can be used to observe the variation in irradiation-induced damage versus depth. Thus, Fig. 3(b) plots the change in the background-subtracted and normalized 631 cm^{-1} signal for an irradiated sample minus the same signal on a virgin sample as a function of depth. The figure clearly shows a sharp increase in the signal as the probe focal point scans into the irradiated zone, with the signal maximum occurring when the focal point is centered in the stopping range at a position predicted by Stopping and Range of Ions in Matter (*SRIM)* Monte Carlo simulations [21]. The intensity drops quickly when the focal point is one Rayleigh length beyond the stopping region and then remains at a nearly constant level; this signal level is the same intensity as is seen in a virgin sample. For comparison, the inset shows the depth plot of the 631 cm^{-1} peak area normalized to the area of the active 581 cm^{-1} mode. Note that the maximum is also in the ion-stopping-range region. In the figures below, we use intensity to denote either the absolute Raman intensity or the normalized background-subtracted signal.

Figure 4 shows the normalized intensities of the 631 cm^{-1} Raman mode after irradiation in three samples, each at a different ion energy. The data shows that as the ion energy is decreased, the stopping ranges of the He^+ ions are progressively closer to the surface. The dotted lines in the figure give the calculated stopping ranges using *SRIM* simulations; see Table 1. The experimental and the *SRIM* peak positions agree closely. Note that the peaks widths are related to the straggle distribution at each ion energy – higher energy ions sensibly result in larger straggle, that is, a broader peak width of the mode. A measurement of the variation in the intensity versus depth shows that the Z-resolution of these measurements is limited by the depth of focus of the Gaussian laser beam. The Rayleigh length in the system is approximately ~2 μm. This limitation on depth resolution also results in inhomogeneous broadening of the features seen with the Raman probe. However, it should be emphasized that despite its limited resolution, depth scanning is the quickest and easiest of the three optical configurations for examining radiation damage.

#180352 - $15.00 USD Received 26 Nov 2012; revised 14 Dec 2012; accepted 15 Dec 2012; published 21 Dec 2012

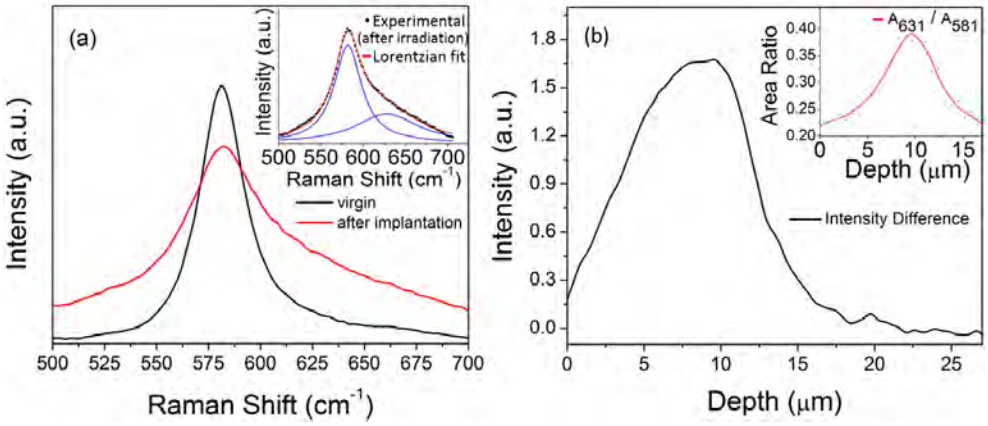

Fig. 3. Examples of irradiation damage measured using the depth scan optical configuration over the 500 to 700 cm^{-1} spectral region: (a) comparison of peak shapes before and after irradiation, showing the change of the peak width and the appearance of the shoulder in higher frequency region after irradiation; inset: example of Lorentzian peak fitting to resolve the appearance of the normally forbidden 631 cm^{-1} mode besides the active 581 cm^{-1} mode; 3.8 MeV, 5 × 10^{16} cm^{-2} dose. (b) Plot of the intensity of the 631 cm^{-1} mode, in the irradiated sample minus that in the virgin sample, after the subtraction of the respective backgrounds. Note that there is a strong signal in the region of maximum damage or ion range; the signal drops once the focal point of the probe beam is one Rayleigh length deeper than the defect region. The inset shows the integrated-peak-area ratio between 631 cm^{-1} and 581 cm^{-1} phonon modes as a function of the probing depth. It is clear that the maximum is in the ion range region.

Table 1. *SRIM* Simulation Results of Ion Ranges and Straggle for the Ion Energies Given in the Experiments Shown in Fig. 4

Energy	Ion Range	Straggle
1.2 MeV	2.81 μm	212 nm
3.0 MeV	7.65 μm	359 nm
3.8 MeV	10.47 μm	446 nm

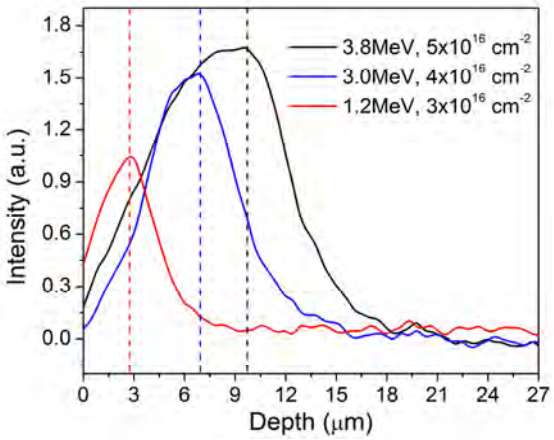

Fig. 4. Depth-profile analysis of the normalized 631 cm^{-1} intensity of the implanted sample less that for the virgin sample; data obtained with depth scanning. The peaks shift toward the surface as the irradiation energy is decreased. The dashed lines indicate the positions of the stopping range for the three different energies as simulated by *SRIM*. Note that the depth read from the scanning stage is corrected, as is described in the text, for the change in focus in the high-refractive-index crystal.

#180352 - $15.00 USD Received 26 Nov 2012; revised 14 Dec 2012; accepted 15 Dec 2012; published 21 Dec 2012

Previous research using nuclear reaction analysis in our group [5] has shown that irradiation can result in a drop in lattice Li concentration in the stopping region, which contains large concentrations of displaced atoms and He interstitials. In addition, prior Raman experiments [22–24] have shown that the lowest frequency E(TO_1) 152 cm^{-1} mode is sensitive to the Li content in $LiNbO_3$; this sensitivity plus its linear response suggests its use as a probe of the local Li-lattice-atom concentration for our experiments. With this information in mind, we carried out a depth scan of the irradiated region using the 152 cm^{-1}-shifted Raman signal. Figure 5 shows the data from that measurement; it is clear that the Li composition decreases after irradiation. In particular, there is a difference in the normalized intensity between the virgin and irradiated sample. In addition, the data shows that irradiation caused a decrease in intensity in the neighborhood of the stopping region (see the inset); this loss is attributed in part to the loss of Li.

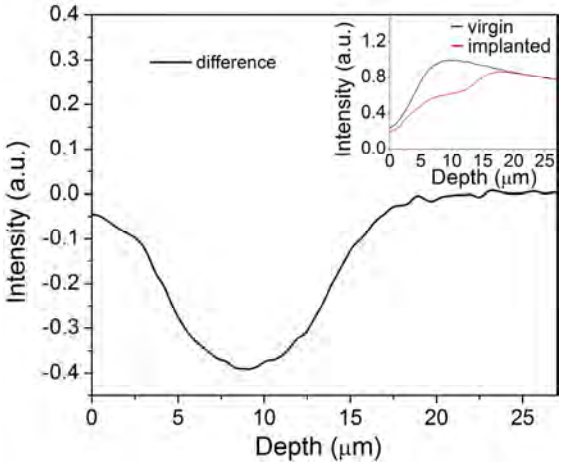

Fig. 5. Depth profile analysis with respect to the E(TO_1) 152 cm^{-1} Raman mode obtained with a depth scan. For the He^+-irradiated $LiNbO_3$ (3.8 MeV, 5×10^{16} cm^{-2} dose), there is an intensity drop in the stopping range and straggle region indicating that concentration of Li was reduced.

Prior studies in our group and others have shown that low-temperature annealing of an irradiated sample can alter the effects of radiation damage. Specifically, we have shown [20,25] that during He^+ irradiation, the high-density of point defects and He atoms inserted into the crystal lattice lead to the formation of clustering of defects, including, at high dose, He bubble formation. In fact, our earlier experiments showed that there was a threshold D_t for which the concentration of the generated vacancy-interstitial pairs are high enough to form a defect network. In addition, these results indicated that the He inclusions become mobile at elevated temperatures. In addition, TEM imaging studies show that at higher temperature (350°C), the inclusions aggregate together to form larger defects. Avrahami *et al*. [26,27] used high-resolution X-ray diffraction to reveal that He-ion irradiation results in lattice swelling. Thus for a dose of ~10^{16} cm^{-2}, the profile of induced strain as a function of depth was found to approach a step-like shape with the strain increasing abruptly at the ion range; in addition, annealing at temperatures above 200°C was found to lead to partial recovery of the crystal lattice.

We have used micro-Raman spectroscopy to find a dependence on dose and annealing conditions, which is consistent with the above experiments of annealing in irradiated crystals. In particular, after annealing of an irradiated crystal, our Raman microprobe was used to study the 631 cm^{-1}-mode signal versus dose and annealing temperature (see Figs. 6(a) and 6(b)); the duration of the annealing process was 30 min for all the experiments. Our experiments showed that signals from the broadband shoulder are seen only when the dose is >10^{16} cm^{-2} (Fig. 6(a)). The existence of this threshold dose is attributed to a nonlinear dependence on the local concentration of ion-induced defects. Insight into this threshold behavior can be obtained

#180352 - $15.00 USD Received 26 Nov 2012; revised 14 Dec 2012; accepted 15 Dec 2012; published 21 Dec 2012

via earlier work by Schrempel *et al*. [28]. In these experiments Rutherford backscattering spectrometry (RBS) at 1.4 MeV He^+-ions was used to show that for doses greater than ~10^{16} cm^{-2}, the relative defect concentration increased abruptly. This increase was explained by the formation of heavily damaged defect clusters. Note *TRIM* simulation shows that a 1.5 MeV He^+ irradiation to a dose of 10^{16} cm^{-2} causes a total vacancy concentration of 10^{22} cm^{-3}, or ~0.25 dpa (displacement per atom), thus indicating a very high degree of damage in the implantation area at this ion fluence.

In addition, in separate experiments, the effects of annealing on a heavily irradiated sample were examined. One example of a set of such measurements is shown in Fig. 6(b) for a sample irradiated at 3.8 MeV to a total dose of 5 × 10^{16} cm^{-2}. As shown in Fig. 6(b), annealing reduces the intensity of the 631 cm^{-1} feature. The intensity of the feature, minus that in the virgin sample, can be plotted versus the inverse energy so as to extract a characteristic activation energy for the process. This result is shown in the inset of Fig. 6(b); the plot shows an Arrhenius-like behavior with E_a = 0.32 ± 0.07 eV. This activation energy is similar to the value measured by XRD [27] of E_a = 0.32 ± 0.03 eV. This similarity suggests that the emergence of the mode is related to swelling of the lattice spacing after irradiation. More generally these results show that annealing can enable recovery of the crystalline quality of heavily irradiated crystals.

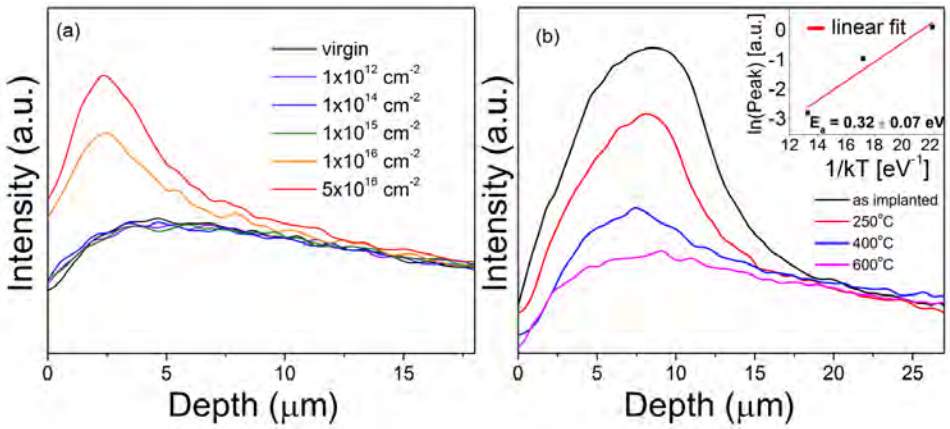

Fig. 6. (a) The intensity of the 631 cm^{-1} feature with depth scanning *vs.* irradiation dose of 1.5 MeV He^+ ions. A signal is seen only when the dose is >10^{16} cm^{-2}. (b) Effect of annealing for 30 minutes at different temperatures on the peak intensity of 631 cm^{-1} following irradiation at 3.8 MeV to a total dose of 5 × 10^{16} cm^{-2}. This change is due to annealing-induced recovery of damage. The inset shows an Arrhenius plot of the peak intensity irradiated sample relative to that for the virgin sample for T [3] 250°C, which gives an activation energy of 0.32 ± 0.07 eV.

We now address the other modes seen in Fig. 2. Kong *et al.* [29] reported that for nonstoichiometric $LiNbO_3$ crystals, a weak Raman peak is present at ~738 cm^{-1} Raman shift due to the formation of an ilmenite-defect phase. This same feature is seen in our measurements of the virgin sample and is unchanged in the irradiated and annealed samples, as is seen in Fig. 2; this peak is enlarged in Fig. 7 and fit to a Gaussian profile. Note that for this spectral feature, a Gaussian lineshape fits better than a Lorentzian profile, a result expected given the more inhomogeneous distribution of the intrinsic defects in congruent $LiNbO_3$. In ion-irradiated samples, a new peak is seen for a ~766 cm^{-1} shift, only when the dose is above the threshold (~10^{16} cm^{-2}). Its intensity, determined using the curve fitting shown in (a), decreases with annealing, as shown in (b). The activation energy for annealing, as ascertained by the decrease of this peak with temperature, is E_a = 0.30 ± 0.05 eV. This value is consistent with that determined above in Fig. 6, suggesting again the emergence of this mode is also related to irradiation-induced inhomogeneous lattice expansion.

#180352 - $15.00 USD Received 26 Nov 2012; revised 14 Dec 2012; accepted 15 Dec 2012; published 21 Dec 2012

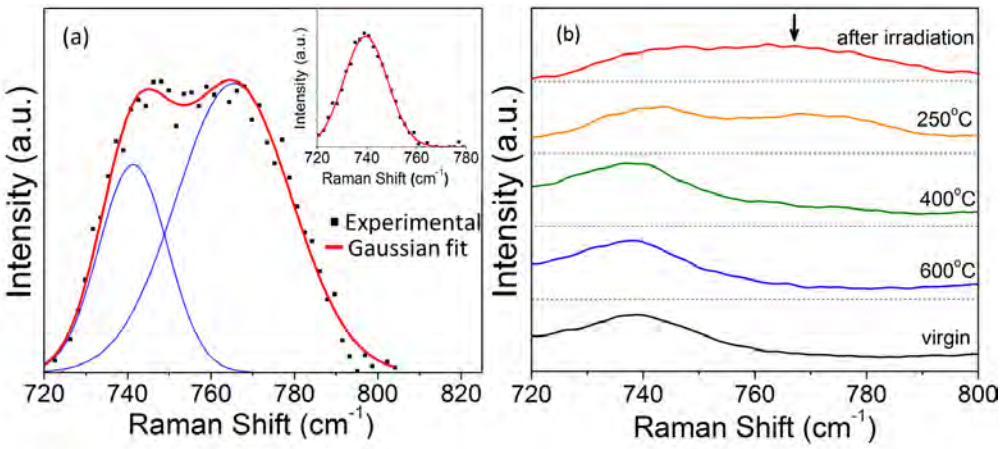

Fig. 7. (a) Raman spectra of a defect mode in nonstoichiometric $LiNbO_3$ at ~738 cm^{-1}, which is attributed to an ilmenite-like stacking defect in the virgin sample, and an irradiation-induced mode at about 766 cm^{-1}. The sample was irradiated by 3.8 MeV He^+ to a dose of 5×10^{16} cm^{-2}. For comparison, the inset shows the 738 cm^{-1} mode in the pristine sample in the absence of irradiation. The points are the experimental data and the curves are Gaussian fits after a linear background is subtracted. (b) Effect of annealing for 30 minutes at different temperatures on the recovery of damage of the peak intensity of ~766 cm^{-1} (shown by the arrow). The spectra have been vertically displaced for clarity. The activation energy of the annealing process is E_a = 0.30 ± 0.05 eV.

In addition, 2D Raman mapping was utilized to image the damage distribution in a sample with patterned irradiation. To carry out patterning, a 0.5 mm-thick metal sheet with circular-grid openings was placed on the sample top surface so that only the circle regions (with diameters of ~500 μm) were exposed to the He^+ irradiation (3.8 MeV energy and 5×10^{16} cm^{-2} dose). Figure 8(a) shows an optical image of the irradiation pattern, with the Roman numerals (I) and (II) indicating the regions that are irradiated and not irradiated, respectively. Figures 8(b) and 8(c) are examples of 2D Raman image maps of the allowed (875 cm^{-1}) and forbidden (631 cm^{-1}) modes, taken at the depth of the stopping region, i.e. ~10 μm. As discussed previously, the crystallinity of $LiNbO_3$ is damaged in the irradiated regions such that there is an intensity loss for active modes and a gain for the normally forbidden modes. In the unirradiated, masked regions, the crystal quality remains unaffected and thus only the active modes dominate. This behavior results in the high-contrast maps shown in the figures.

A second set of 2D images of the irradiated regions, denoted by (I) and having even finer resolution over a smaller scan distance, were taken at several locations to examine the uniformity of the implantation process. These results show high uniformity of radiation damage based upon the measured standard deviation of the signal intensity. For example, Figs. 8(d) and 8(e) show a set of typical Raman images from a square of 10 μm × 10 μm with a 0.4- μm-step resolution, which were collected using the 875 cm^{-1} active and the 631 cm^{-1} normally forbidden modes. It is clear that when the scan area is away from the implantation boundary, the signals from irradiated regions are uniform, with a standard deviation in the normalized intensity of ~0.010 for the 875 cm^{-1} mode and ~0.015 for the 631 cm^{-1}mode, respectively. These results indicate that the patterned implantation process is in general uniform.

Figure 8 also shows that the shapes of the Raman images conform well to the overall irradiated pattern. Our Raman probe can also be used to examine the details of the boundary region at the edge of the masked regions. A higher resolution area mapping of a 16 μm × 16 μm square region was carried out. The Raman imaging using the 875 cm^{-1} and 631 cm^{-1} modes is displayed in Figs. 9(a) and 9(b); (c) is a line scan across the edge of the mask, as indicated by the arrows in (a) and (b). Region (I) is irradiated while region (II) is masked. In

#180352 - $15.00 USD Received 26 Nov 2012; revised 14 Dec 2012; accepted 15 Dec 2012; published 21 Dec 2012

addition, we notice that in the region with smaller higher resolution, a transition region is apparent near the boundary, as denoted by (III). We attribute this transition region to the masking procedure for this patterned irradiation. The lack of full adhesion of the mask to the surface results in a gradation in the irradiation damage in the boundary region. In addition, in this region He^+ scattering from the mask edge also contributes to a ~4% increase in the radius of the irradiated region compared to the radius of the mask opening.

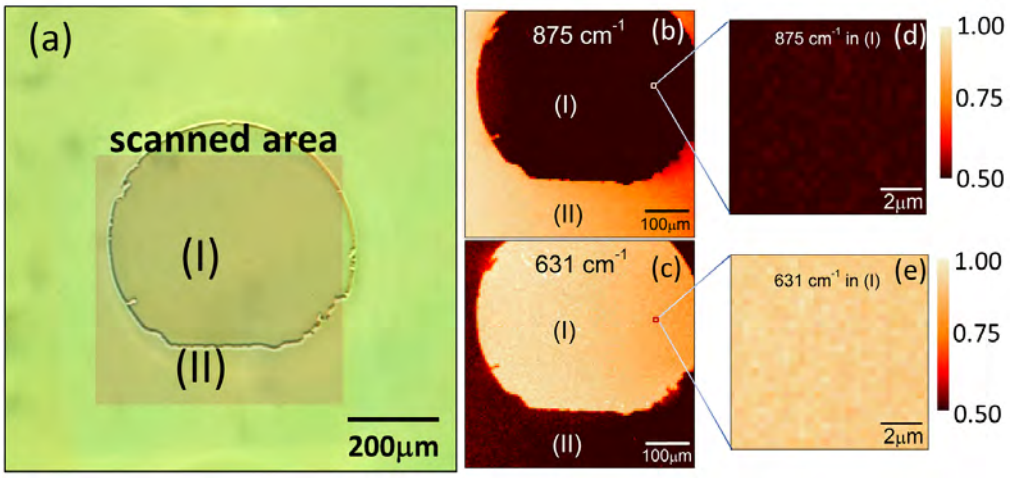

Fig. 8. 2D Raman images showing the intensity variation of two Raman modes after irradiation of a masked sample. The patterning of the ion beam (3.8 MeV He^+, 5×10^{16} cm^{-2} dose) utilized a shadow mask consisting of a metal circular grid affixed to the sample. The optical image (a) labels the regions being with or without irradiation (regions I and II, respectively). The inset box indicates the region where the Raman imaging was carried out. In (b) and (c), the Raman maps were analyzed using an allowed (875 cm^{-1}) and forbidden mode (631 cm^{-1}). In the irradiated regions the signals of active modes decrease while the forbidden modes are "turned on", respectively, due to irradiation-induced crystal disorder. In (d) and (e), a finer and smaller scan was performed and the results show that the patterned implantation process was uniform.

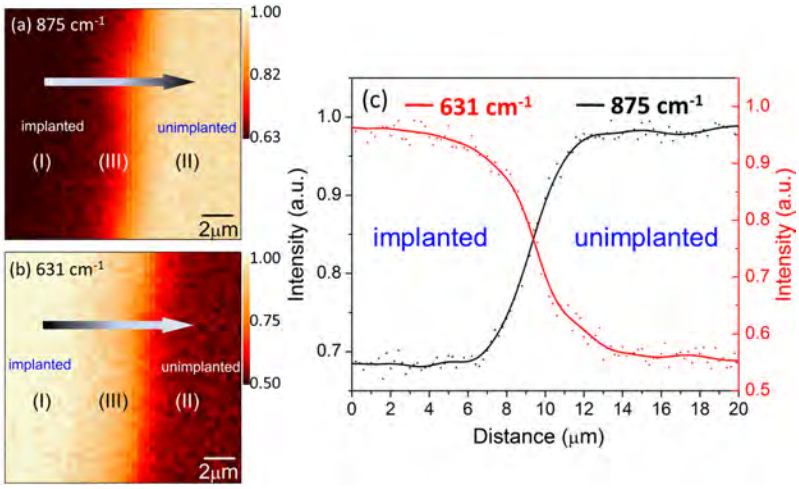

Fig. 9. Fine spatial resolution of Raman mapping of a defect region in a patterned sample. Panels (a) and (b) show 2D scans of the active 875 cm^{-1} and normally forbidden 631 cm^{-1} modes, with scan step of 0.4 μm, respectively, while (c) is a line scan across the boundary, as indicated by the arrows in (a) and (b), with a scan step of 0.2 μm. From (c), it is clear that the signals of the two modes decrease/increase within a specific width of the boundary, denoted by (III) in (a) and (b), and stay uniform outside the transition regions, marked by (I) and (II). The data have been normalized with respect to their maximum values.

#180352 - $15.00 USD Received 26 Nov 2012; revised 14 Dec 2012; accepted 15 Dec 2012; published 21 Dec 2012

3.2. Data obtained from probing across the edge facet (edge scan)

Radiation damage was also probed via scanning across an end facet, using the geometry shown in Fig. 1(b). A different set of selection rules applies for this optical configuration as compared with those used in the depth-scanning configuration. Figure 10 shows representative Raman spectra from the near-surface region, at the position of the ion stopping region and at a point deep within the virgin region of the crystal; the locations are specified in the optical image to the right of the spectra. Examining first the $A_1(TO_4)$ 631 cm^{-1} mode, its peak intensity weakens and broadens as the scan probes close to the region of expected irradiation damage. Note that this mode shows some evidence of a red shift as the beam is scanned closer to the heavily damaged region; this shift is tentatively attributed to strain. From 800 to 900 cm^{-1}, additional spectral features emerge when the beam interrogates the sample close to the stopping range. These features appear to originate from irradiation-induced activation of the $A_1(LO)$ mode at 875 cm^{-1}, which is forbidden for the perfect crystal in this beam configuration. A contribution from the E(LO) forbidden mode at 880 cm^{-1} is also possible, although its effective Raman scattering cross section is much less than that of the $A_1(LO)$ 875 cm^{-1} mode [30]. The observation of this band was previously briefly noted by Kostritskii *et al.* [14].

The change in the Raman signal with distance along the scan direction is seen in Fig. 11. In particular, the plot shows the peak intensity of the irradiated sample minus that of the unirradiated sample for the $E(TO_1)$ 152 cm^{-1} and $A_1(TO_4)$ 631 cm^{-1} active modes and the $A_1(LO)$ 875 cm^{-1} forbidden mode versus distance. It is seen that irradiation results in the rise of the previously forbidden modes and a decrease in the signal of the active mode, with the maximum/minima of this effect occurring at the stopping range (~10 μm).

It is useful to compare the data obtained using this geometry with the results obtained by depth profiling from the top surface. For our data measured when scanning across the end facet, the spectral widths are narrower, due to the narrow width of the stopping region, i.e. ~0.5 μm, and the higher spatial resolution possible in this case. This higher spatial resolution is possible given the 0.5-1 μm spot size of laser as compared with the ~2 μm Rayleigh length, which determines spatial resolution for scanning along the Z direction. In Fig. 11, it is clear that the profiles have much longer "tails" toward the surface than is predicted from the negative skew [31] (i.e. the most probable depth of He^+ ions is greater than the mean depth) obtained from *SRIM* simulation. Thus for the data in Fig. 11, with irradiation conditions 3.8 MeV and 5×10^{16} cm^{-2} He^+ dose, the calculated full width of the ion distribution is ~1 μm. Our data, however, show an effective width of ~3 μm due to this tail. Jamieson *et al*. [11] also observed this same long-tail phenomenon in diamond. The origin of this apparent extension of the damaged region toward the surface that is far greater than that predicted from *SRIM* is unclear at present. Irradiation-induced strain could lead to this effect and measurements of shifts in the Raman spectra indicate that some strain is present. But the fact that the normally allowed mode ($631 cm^{-1}$) is strongly quenched would suggest that more than strain is present.

#180352 - $15.00 USD Received 26 Nov 2012; revised 14 Dec 2012; accepted 15 Dec 2012; published 21 Dec 2012

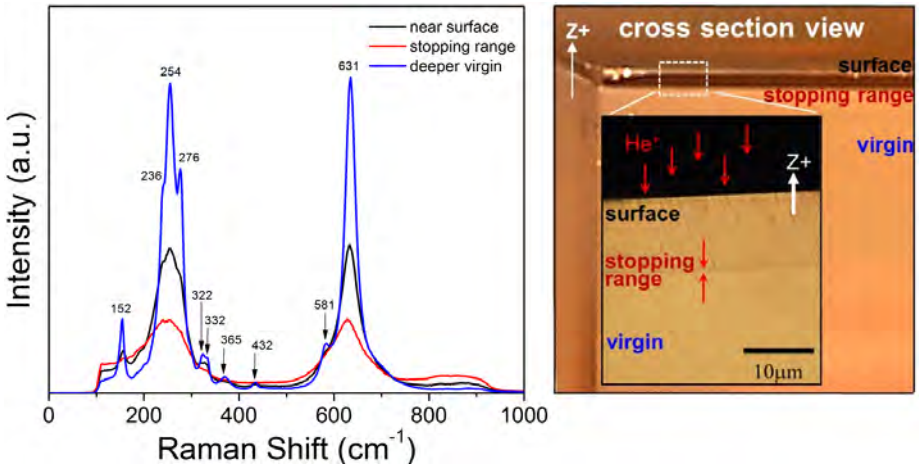

Fig. 10. Raman spectra obtained from an edge scan at three depths from the surface: in the near surface, at the ion stopping region, and deep in the bulk, where there is a negligible effect of irradiation (shown in the optical image to the right). The sample was irradiated by 3.8 MeV He^+ with a dose of 5×10^{16} cm^{-2}. Note the intensities of the active modes drop and the appearance of a shoulder in the 800 to 900 cm^{-1} region.

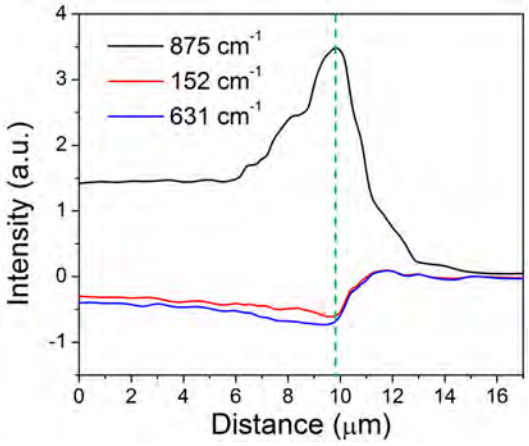

Fig. 11. A plot of signal versus distance using scanned distance from the edge of the top surface for three modes. The sample was irradiated by 3.8 MeV, 5×10^{16} cm^{-2} He^+ doses. For all three curves the maxima or minima of the intensities (relative to those in the virgin sample) occur at the position of the ion range, which is a depth of ~10 μm (shown in dashed line).

3.3. Increasing resolution by edge beveling (bevel scan)

To detect the lateral variation of damage with higher spatial resolution, we examined irradiated samples with a beveled top edge (5° off the XY plane) using the configuration of Fig. 1(c). This off-cut orientation is useful since it allows spatial spreading of the relatively narrow, i.e. 0.5–1 μm, stopping region across an oblique shallow angle, thus expanding the stopping region over a ~10 × larger spatial scale. Thus for a finite beam size, which is larger than the stopping region, this oblique cut enabled higher resolution of the stopping region. Note that a beveled structure is commonly used also in semiconductor materials to study narrow-width doping concentration profiles [32]. Figure 12 shows an optical and SEM micrograph showing the defect network at the stopping range using a beveled sample. In addition, previous work using TEM in our group [20,25] has shown that ion irradiation produces dislocations along the Z axis. The SEM image in Fig. 12 shows that the extended

#180352 - $15.00 USD Received 26 Nov 2012; revised 14 Dec 2012; accepted 15 Dec 2012; published 21 Dec 2012

parts of the line defect at the Z + surface, shown in the optical image, are actually buried below the surface, and the width of the damaged region is in accord with the straggle in the ion stopping distribution in the damaged layer. Before examining irradiated $LiNbO_3$ samples, the micro-Raman spectrum of the 5°-polished plane of an unirradiated sample was compared to that from the XY plane. This experiment determined that these spectra (not shown) are identical, thus indicating that the polishing process and the small angle bevel do not perceptibly affect the Raman spectra.

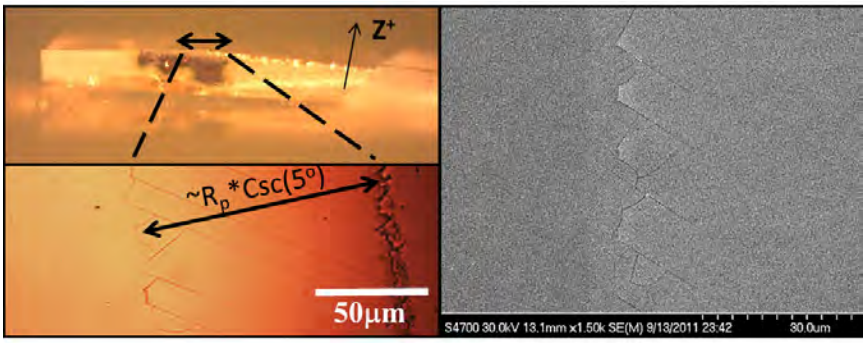

Fig. 12. The optical images (left) and SEM picture (right) show the defect network in the stopping range. The sample was irradiated by 3.8 MeV He^+ to a dose of 5×10^{16} cm^{-2}. This implant energy gives a projected range R_p~10 μm. Our optical image on the beveled plane shows the distance of the defect network to be ~115 μm from Z + surface edge to the deepest extent of the stopping region, which agrees well with *SRIM* calculation of the stopping range (10 μm * csc(5°) ~115 μm).

A scan was then made along the beveled surface and the peak intensity of the 631 cm^{-1} mode (normally forbidden mode) measured as a function of distance laterally across the polished plane of an irradiated sample (3.8 MeV, 5×10^{16} cm^{-2} He dose). These data are displayed in Fig. 13 as the difference in the intensities of the irradiated and virgin samples. Note that as anticipated the beveled geometry with its small slant angle should cause the damage region to be spread out over a larger scan distance, i.e. it is spread by csc(5°) ~11.5, to a scan distance of ~11.5 μm, which is in close agreement with the measured FWHM ~10 μm, see Fig. 13(a). The profile is asymmetric, as is expected given the large tail extending toward the surface described above. Note that the data in Fig. 13(a) contain four additional peaks; the origin of these four peaks is discussed in the next paragraph.

Prior research on ion-irradiated $LiNbO_3$ has shown that line defects are obtained after ion irradiation [20]. This research has shown that in addition to line defects, meandering line defects connecting the straight ones are also observed after mild thermal stressing. These line defects are distributed within a planar layer in the straggle range. In our experiments, these defects are readily seen in our thinned stopping regions. In the immediate region of the sample used to obtain Fig. 13(a), no obvious line defects were apparent; although they were observed in optical microscopy of the neighboring regions; see the inset image in Fig. 13(a). The stripe, emphasized by added dashed lines in the image, indicates the "spread-out" damaged region (~10 μm) on the beveled plane, while the red arrow line is the probe-beam scan direction. The average spacing of the curved lines is ~5 μm, as marked by the black arrows in the inset optical image. Again, note that the location and the direction of the scan were carefully chosen such that they did not cross obvious dislocation lines. In Fig. 13(a), besides the broad peak from the damaged region, there are four additional spatial peaks marked by green arrows. These peaks are most likely due to the buried meandering lines, as the spacing between the rightmost and leftmost two peaks corresponds well to the separation seen in the optical visible lines (i.e. ~5 μm). Thus, the arrows in the figure indicate where these meandering line defects are located. Notice that use of the Raman probe allows ready detection of defect lines, which are otherwise unobservable by visible light microscopy. Also due to the shallow-angle beveled edge, the spatial resolution and the structure of the line defects is enlarged.

#180352 - $15.00 USD Received 26 Nov 2012; revised 14 Dec 2012; accepted 15 Dec 2012; published 21 Dec 2012

These line defects can lead to strong micro-Raman signals and thus one must take care in interpreting the spectral signal in the presence of these defects. For example, Fig. 13(b) shows the result from a line scan in the region where the defect lines were clearly defined in visible microscopy. A broad peak from the spread damage and another three sharp spatial peaks (A, B, and C) were seen, with these three peak positions corresponding to the lines labeled with the letters in the inset image. Unlike Fig. 13(a), the Raman signals from these obvious line defects are so strong that the information from the broad straggle region is obscured. By fitting the peaks with Gaussian profiles, one can extract the width of the straggle region; this value agrees well with the width obtained in Fig. 13(a), taking into account the direction of the scan. The stronger signals from the lines indicate the crystal quality changes significantly in those regions. Note that spatial feature B has the highest intensity. This high intensity is a result of the partial exfoliation in this region of the surface; as will be explained in the next paragraph.

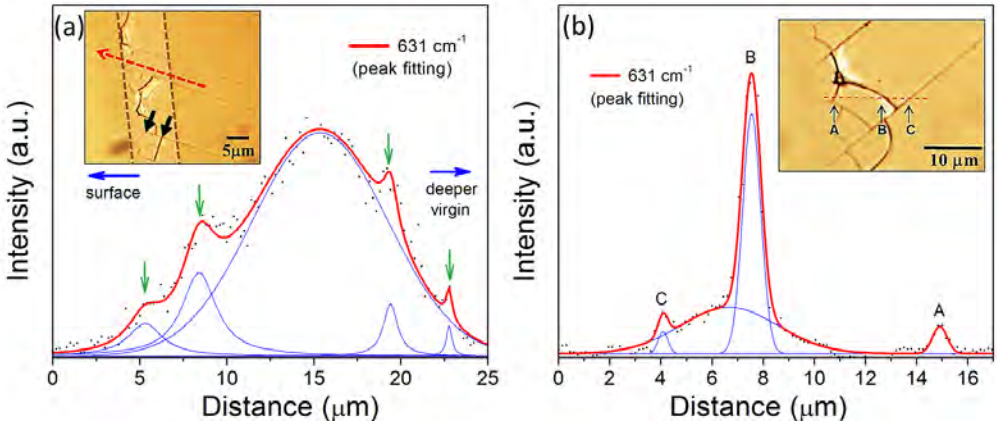

Fig. 13. The intensity of the 631 cm^{-1} mode of the irradiated sample, relative to that from the virgin sample, as a function of lateral position, using a bevel scan. (a): the scan direction was carefully chosen such that no obvious dislocation line defects were crossed. Note that the width of the heavily damaged stopping region is now spread over 10 μm due to the beveled edge. The two black arrows in the inset optical image indicate positions of typical dislocation line defects; the relative widths of these features are discussed in the text. (b): Besides the broad peak from the spatially spread-out damaged region, three additional spatial peaks (A, B and C) are observed. These narrow peaks occur when the scan crosses a line defect as a result of changes in the sample crystallinity in this region.

One potential difficulty with the off-cut angle-polishing approach is that in a heavily irradiated sample there is possibly distorted edge surface region. The distortion in this narrow region is due to the blistering and micro-cracks, which are known at high irradiation doses. Thus Primak [33] pointed out that at a dose of ~10^{16} cm^{-2}, surface deformation and destruction were observed on the stopping plane when using lower energy ions than in our case, *i.e.* 140 keV *vs* 3.8 MeV. In our experiments, when the dose is above 1 × 10^{16} cm^{-2}, exfoliation occurs on the polished plane, while surface quality of the XY plane remains as seen in optical microscopy, see panels (a) and (c) in Fig. 14. Since this damage concentration is high, surface crazing readily appears in the stopping range upon polishing; this effect is seen clearly in (c). Presumably due to the stress in the damaged region, heating of the irradiated crystal can lead to additional damage. Thus panels (b) and (d) show that after further annealing additional micro-domains become apparent (see [22]) in the top view (XY plane) of panel (b) and in addition, the incipient exfoliation in panel (d) has progressed noticeably.

#180352 - $15.00 USD Received 26 Nov 2012; revised 14 Dec 2012; accepted 15 Dec 2012; published 21 Dec 2012

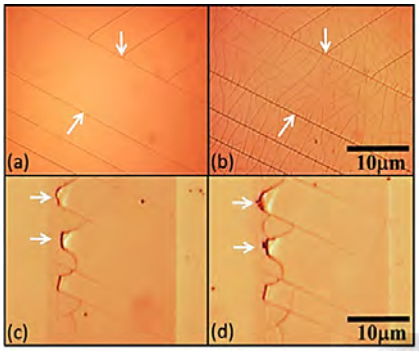

Fig. 14. Optical imaging showing the effect of annealing at 250°C: (a), (b) are top views (XY plane [22]) while (c), (d) are planes of beveled region. Figures (a) and (c) were taken before annealing, while (b) and (d) were taken after annealing.

The change in morphology in the polished region can lead to major changes in the overall Raman spectra and result in spurious effects. For example, Fig. 15 shows the data taken at four focal point locations on the surface: A, B, C, and D; see the optical image and schematic for beam/sample geometry. A is the point on the tip of the blistering while B and C are spaced by 0.5 μm. D is the furthest point from the stopping range, ~5 μm. It is clear that the spectra are very different. First, the spectrum at point D resembles that collected from the top-down scanning method: the E(TO) and A_1(LO) modes are observed via the appearance of weak shoulders from 600 to 700 cm^{-1}. As the Raman probe scans close to the ion range (points C and B), the A_1(TO) mode signals also appear, with the intensity being highest at edge (point A). The inset in Fig. 16 contains an image of the spatial distribution of the $A_1(TO_4)$ 631 cm^{-1} mode obtained in the neighborhood of the stopping range. This analysis indicates that the 631 cm^{-1} mode intensity is the greatest (shown in green) along the edge of the exfoliated region and that it decays quickly once the scanning moves off of this edge region. We attribute this high intensity to the strong crystal disorder in the ion stopping region, as mentioned above. But, in addition, we also note that in this region of the crystal we expect additional light coupling and some degree of local light guiding of the probe beam. In particular, due to the blister-induced raising or exfoliation of the crystal edge local light guiding can occur; see the lower inset in Fig. 16. This effect may alter the local light/crystal coupling and give rise to additional modal structure such as the appearance of A_1(TO) modes.

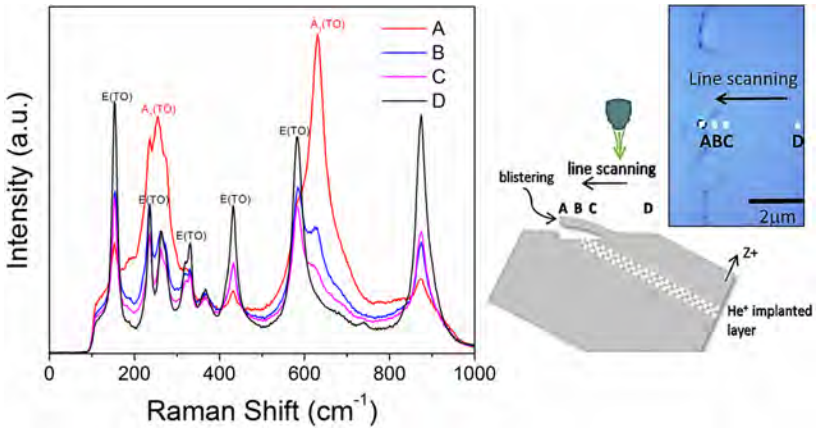

Fig. 15. Micro-Raman spectra on an irradiated sample by scanning on a 5° beveled polished plane. The optical image shows the location of the probe beam focal point. In going from point D to B the probe successively probes regions of greater ion-beam irradiation. Note that the data obtained at point A is distorted by local light guiding/coupling into the partially exfoliated region.

#180352 - $15.00 USD Received 26 Nov 2012; revised 14 Dec 2012; accepted 15 Dec 2012; published 21 Dec 2012

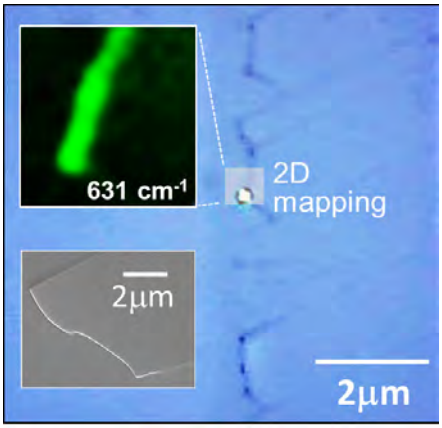

Fig. 16. Micro-Raman area mapping in the neighborhood of the stopping range. The 2D intensity analysis of the 631 cm^{-1} peak (the upper inset) indicates that the peak reaches a maximum at the edge of the blister/exfoliation region and drops quickly when the beam scans away from this region. The lower inset is an SEM imaging showing the blistering in the stopping range of the polished plane. The raised sample edge is indicative of partial exfoliation.

4. Conclusions

In conclusion, we have used micro-Raman spectroscopy to diagnose and image damage in oxide crystals following high-energy ion irradiation and have demonstrated that it is a powerful and versatile approach. In particular, we have used vibrational Raman scattering on He^{+} irradiated $LiNbO_3$ samples to observe the effects of local damage in both allowed and forbidden modes, local Li-atom depletion, and the spatial distribution of damage. We show, for example, there is a threshold dosage, for which the lattice distortion is apparent and that annealing is important for recovering the sample crystallinity.

Furthermore, we have found that complementary information can be obtained from three Raman micro-probe configurations and preparation methods, due to their different geometries, spatial resolution, and polarization sensitivities. Depth-dependent damage data can be obtained most readily and in a nondestructive manner by scanning along the Z-axis (depth scan). While this scan direction gives qualitative and useful information, it requires no additional sample preparation, and is very suitable for *in situ* or real time analysis of the degree of crystallinity during processing, it has limited spatial resolution. Scanning along a polished or cleaved edge is an alternate approach (edge scan), but, while it permits probing different modes, the narrow spatial dimensions on the edge compared to the laser-spot size limits spatial resolution. Scanning on the beveled plane (bevel scan) provides the best spatial resolution and information regarding dislocation line defects and surface morphology of the irradiated sample, but the sample preparation process is, of course, somewhat more complex and care must be taken to guard against changes in morphology in the thinned region of the sample edge during polishing. Finally, we have shown the utility of 2D imaging in probing the resolution of a patterned, irradiated sample and examining the uniformity of irradiation-induced effects and damage profiles and insight into the nature of the ion-induced local degradation of the crystal.

Acknowledgments

The authors gratefully acknowledge useful comments and discussions with Prof. Aron Pinczuk and Dr. YuMeng You and with Profs. John Kymissis and Dirk Englund. This work was supported by the Department of the Defense, Defense Threat Reduction Agency (DTRA) under HDTRA1-11-1-0022.

#180352 - $15.00 USD Received 26 Nov 2012; revised 14 Dec 2012; accepted 15 Dec 2012; published 21 Dec 2012